Department of Physics and Astronomy

University of Heidelberg

Bachelor Thesis in Physics

submitted by

Leander Fischer

born in Heidelberg

2016

Investigation of Material Coatings in order to Reduce the Emanation of Radon

This Bachelor Thesis has been carried out by Leander Fischer at the

Max-Plank-Institut für Kernphysik in Heidelberg

under the supervision of

Prof. Dr. Manfred Lindner

Zusammenfassung

Die Beobachtung von Wechselwirkungsprozessen in Experimenten mit sehr geringer Ereignissrate benötigt eine außerordentliche Nachweisempfindlichkeit. Um dies zu erreichen, ist eine wesentliche Reduktion des Untergrundes notwendig. Das XENON1T Experiment verwendet flüssiges Xenon als Targetmaterial für Streuprozesse von massiven, schwach wechselwirkenden Teilchen (engl. "WIMPs"), die einen bevorzugten Kandidaten für *dunkle Materie* im Universum darstellen. Das radiaktive Radon Isotop ^{222}Rn ist eine der bedeutendsten Untergrundquellen, da es permanent aus den verwendeten Detektormaterialien emaniert. Da sich Radon als Edelgas gleichmäßig im flüssigen Xenon verteilt, können die Zerfälle seiner Tochterisotope überall das gesuchte Signal imitieren. In dieser Arbeit wurde ein experimenteller Aufbau zur Messung der Radon Emanation benutzt um zu untersuchen, wie sich das Emanationverhalten eines kontaminierten Materials verhält, wenn es beschichtet wird. Unterschiedliche Beschichtungsverfahren und Materialien wurden getestet und die Ergebnisse werden diskutiert. Das Gesamtergebnis in Form des Reduktionsfaktors wird angegeben und die darausfolgende mögliche Verbesserung des Untergrundes des XENON1T und XENONNT Detektors abgeschätzt. Desweiteren wurde die Detektion von ^{222}Rn mithilfe der miniaturisierten Proportionalzählrohre verbessert, indem die exakte Detektionseffizienz von Radon und seinen Tochterisotopen bestimmt wurde.

Abstract

Dark matter direct detection experiments require a substantial background reduction to reach the sensitivity needed for the observation of interaction processes with very low event rates. The XENON1T experiment uses liquid xenon as a target material for scattering events of Weakly Interacting Massive Particles (WIMPs), that are favoured candidates as particle *dark matter*. The radioactive isotope of radon (^{222}Rn) is one of the most serious intrinsic background sources, since it can be emanated from all materials in the detector. As a noble gas, it is distributed homogeneously inside the liquid xenon, where the subsequent decays of its daughter isotopes can mimic the expected WIMP signal. In this thesis, an experimental setup to measure radon emanation is employed to study the effect of coating on a contaminated material to prevent radon from emanation. Different coating techniques and materials are analysed and the individual results will be discussed. The final result of the emanation reduction achieved by coating will be shown, with an estimation on the improved radon background of XENON1T as a possible application for XENONNT. Additionally, a set of measurements was done to further improve the detection of ^{222}Rn with proportional counters, by determining detection efficiency for radon and its progenies.

Contents

Chapter 1

Introduction

The Swiss astronomer Fritz Zwicky was the first to make observations that lead to one of the biggest unsolved mysteries in modern physics - the nature of *dark matter*. In 1933, he examined the Coma galaxy cluster and realized that the velocities of the galaxies far from the center were too large to be explained by the gravitational interaction of luminous matter only [1]. Therefore, he concluded that there had to be a large amount of non-luminous, gravitating mass: *dark matter*. Until today many other observations concerning the existence of *dark matter* have been made and there are different theories about its nature. A widely accepted theory is that *dark matter* is composed of Weakly Interacting Massive Particles, the so-called WIMPs.

1.1 Dark Matter

1.1.1 Evidence for the Existence of Dark Matter

After Zwicky found the first evidence indicating *dark matter*, other observations made in the second half of the last century also indicated its existence. The rotation curves of matter in spiral galaxies, as observed by Rubin et. al in 1978, are different from what is expected if there was only the known luminous matter [2]. The conclusion was that there must be an additional mass contribution that increases with the distance r from the galactic center. It is often described as a *dark matter halo*, consisting of the new, non-luminous kind of matter, called *dark matter*. On larger scales, Fritz Zwicky had already observed the gravitational interaction of this new kind of matter between galaxies in galaxy clusters. Gravitational lensing is another technique allowing *dark matter* to be observed on even larger scales. It exploits the fact that matter is capable of bending the path of light. In this way, *dark matter* in astronomical objects can be discovered indirectly by studying the lensing effect of these objects on luminous objects around or directly behind them. The more mass they have, the stronger the lensing effect. The current cosmological model is based on the fact, that *dark matter* exists. Newest observations of temperature anisotropies in the Cosmic Microwave Background (CMB) performed by the Planck

satellite allow the parameters, describing the energy content of *dark matter* in the Universe, to be measured. Modelling the data from the 2013 released data set [3], using a fit based on the ΛCDM[1] model, results in an energy distribution made of 4.9 % baryonic matter, 26.8 % *dark matter* and 68.3 % *dark energy*.

1.1.2 Dark Matter Candidates

Although there are various theories concerning the nature of *dark matter*, describing it as a particle is the most promising. In [4] further information on the various models can be found. A *dark matter* particle would have to fulfil certain conditions. As already implied by the name "*dark*", it should not emit or interact with electromagnetic radiation. On top of that, it has to be non-baryonic (known from CMB) and non-relativistic (*warm* or *cold*). The particle should also be stable or at least have a long lifetime compared to the age of the Universe, to be still present in the Universe today. To explain the gravitational behaviour of galaxies and galaxy clusters, as described in Section 1.1.1, and the observed deflection of light caused by *dark matter*, the particles must interact gravitationally [5]. To find such a particle, we have to go beyond the Standard Model of Particle Physics. A very promising model are WIMPs, referring to electrically neutral, massive particles, which only weakly interact with baryonic matter. The existence of such a particle would theoretically allow its detection on Earth, since our galaxy would also be surrounded by a *dark matter* halo. The aim of the XENON Collaboration is the direct detection of WIMPs through recording the signals produced by a WIMP scattering of a xenon nuclei.

1.2 The XENON Dark Matter Project

In XENON experiments, liquid xenon (LXe) is the detection medium to search for dark matter particles. Xenon is a favoured material because its ionization and scintillation properties allow the detection of WIMPs, a discrimination from background and its boiling point is around -110 °. The experiments are located in the Gran Sasso National Labatory (LNGS) in Italy, where the first experiment XENON10 was deployed in 2006. The advantage of the deep underground facilitiy is that it provides a 3800 mwe (meter water equivalent) rock shielding against cosmic radiation. After XENON10, the XENON100 detector, containing about 165 kg of LXe (∼10 times the amount used in XENON10), was installed in 2008. XENON1T represents the newest phase of the experiment. It is currently under commissioning and will be operated with a total of 3.3 t of LXe. With further background reduction, XENON1T will be able to reach unprecedented sensitivity. In a 2 year live-time, the detector could detect in the order of 100 events assuming $\sigma_{SI} \sim 2 \cdot 10^{-45}\,cm^2$ and a WIMP mass of $100\,GeV/c^2$. If no positive signal is measured, the experiment will exclude cross-sections above $2 \cdot 10^{-47}\,cm^2$ for a WIMP mass of $50\,GeV/c^2$ [6]. There also is a future project called XENONNT, which is an upgrade of the XENON1T detector.

[1] Lambda cold dark matter.

1.2.1 Detection Principle of the XENON1T Detector

The innermost part of the XENON1T detector consists of a two-phase Time Projection Chamber (TPC) (shown in Figure 1.1 (left)). The stainless steel vessel, approximately 1 m high by 1 m diameter, is filled with LXe except for a layer of gaseous Xenon (GXe) on top.

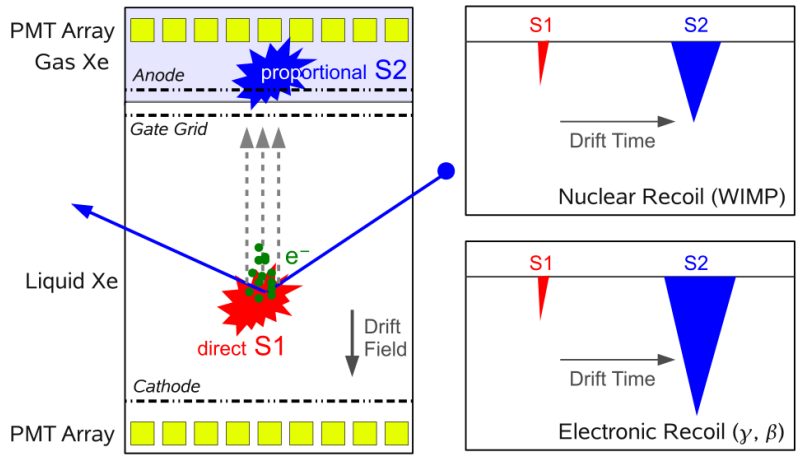

Figure 1.1: (Left) Representation of the working principle of the XENON dual-phase TPC. (Right) Waveform sketch of nuclear and electronic recoil events. Discrimination between nuclear and electronic recoil is possible by comparing the amplitude ratios between prompt scintillation signal S1 and proportional scintillation signal S2. Taken from [6].

Incident particles interact with xenon atoms and can therefore be detected. Neutral particles like neutrons or WIMPs scatter elastically off the xenon nuclei (nuclear recoil), whereas γ-rays or charged particles mostly interact with the orbital electrons (electronic recoil). Both electronic and nuclear recoil cause excitation and ionisation of the xenon atoms. The photons produced by disexcitation can be detected by the 248 Photo Multiplier Tubes (PMTs) at the top and the bottom of the TPC (see Figure 1.1 (left)). The light emitted immediately after the scattering process is called *direct scintillation light*, often referred to as S1. The free electrons from ionization are drifted towards the LXe surface along a drift field, applied between the cathode and the gate grid. When reaching the liquid/gas interface, they are extracted from the LXe by another electric field between the gate grid and the anode. In GXe, the electrons produce a second light signal called *proportional scintillation light* or S2 that can be detected by the top PMT array. The two signals translate into a spatial identification ((x,y)-coordinate) of the scattering event, by evaluating the hit pattern. The time between the detecion of S1 and S2 is proportional to the drift time of the electrons, allowing the reconstruction of the z-coordinate of S1. Knowing the exact place of the scattering event provides an important tool to distinguish signal events from background, that is expected to be located mostly at the edges of the TPC. Additionally, the ratio of the signal amplitudes S1/S2 can be measured (as shown in Figure 1.1 (right)). Since their ratios differ significantly, nuclear and electronic recoils can be discriminated.

To block ambient radiation and reduce neutron background, the detector is placed in a 9.6 m diameter water tank, equipped with 84 additional PMTs detecting Cherenkov light produced by cosmic muons. Muons can mimic *dark matter* signals and the PMTs allow for these events to be rejected. Combining all these methods and before applying the selection to discriminate

between nuclear and electronic recoil, the detector is expected to reach a total electronic recoil (ER) background of $(1.80 \pm 0.15) \cdot 10^{-4}$ (kg·day·keV)$^{-1}$ in a 1 t fiducial volume [7]. This is mainly due to the decay of ^{222}Rn daughters inside the xenon target, as will be discussed in the following.

1.3 Radon induced Background in liquid noble gas detectors

In most particle physics experiments with a very low interaction rate, such as XENON1T and the future upgrade XENONNT, radon is an important intrinsic background source. ^{222}Rn emanation from the detector materials results in a homogeneous distribution of radon within the target material. Radon belongs to the radioactive decay chains of ^{238}U (see Figure 1.2), ^{235}U and ^{232}Th. The isotopes ^{222}Rn and ^{220}Rn have the longest half lives with $T_{1/2}^{Rn222} = 3.82$ days and $T_{1/2}^{Rn220} = 55.8$ s [8], [9].

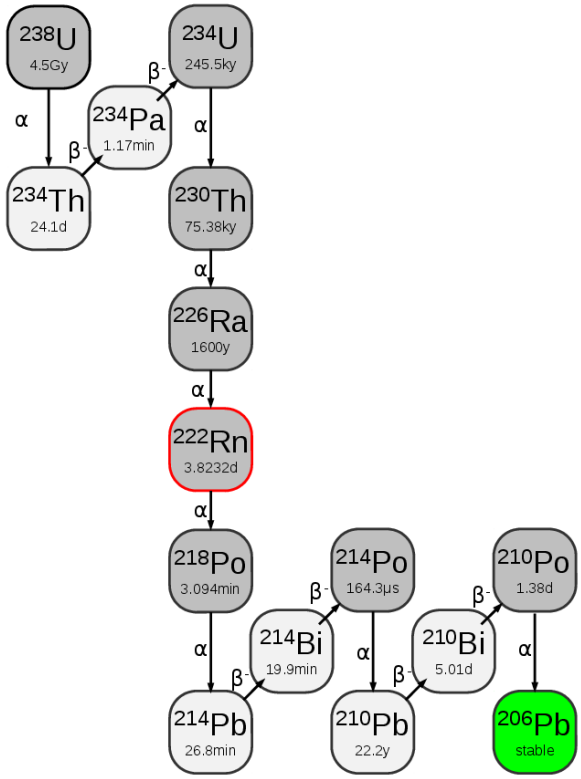

Figure 1.2: ^{238}U decay chain. ^{222}Rn (marked in red) is one of the most important intrinsic background sources for XENON1T.

^{222}Rn is the daughter nucleus of ^{226}Ra and being a noble gas it emanates into the LXe. The emanation process will be explained in more detail in Chapter 3. It is distributed uniformly because of its long enough half-life. This property makes it a critical background, since it reaches the fiducial volume[2] of the detector. According to [10], background induced by ^{220}Rn is suppressed, since it does not reach the innermost part of the detector, due to its shorter half-life. Applying a fiducial volume cut therefore neglects all these events. In the following, "radon" will

[2]In particle physics experiments, a fiducial volume is an inner volume of the detector in which background events are largely excluded.

stand for ^{222}Rn. As can be seen in Figure 1.2, the decay of radon is followed by a series of α and β decays and γ emissions.

The expected WIMP signals in XENON1T are in the energy range below 100 keV [10]. Consequently, only decays in this energy range can be mistaken for signals. The β-decays of the radon progenies show a continuous energy spectrum up to their individual Q-value. From the β-decays of ^{214}Pb, ^{214}Bi, ^{210}Pb and ^{210}Bi, ^{210}Pb turns out to be the strongest contribution [11]. Due to the long half-life, $T_{1/2}^{210Pb} = 22.23\,\mathrm{y}$ [9], of ^{210}Pb, compared to the runtime of the detector, the β-decays of ^{210}Pb and ^{210}Bi can be neglected as background contribution.

The goal for XENON1T was to reach a ^{222}Rn concentration of 1 μBq/kg xenon. A possible way to reduce the radon background is to carefully select the detector materials that are in direct contact with the xenon. This was done in a long screening campaign at the MPIK[3]. As a result, the ^{222}Rn contamination was estimated to be 10 μBq/kg, leading to an ER background of $1.54 \cdot 10^{-4}\,(\mathrm{kg \cdot day \cdot keV})^{-1}$ in the [1, 12] keV region, in a 1 t fiducial volume [10]. This accounts for ∼85% of the total ER background. The reason for this high contribution is that even the most radio-pure materials are still slightly contaminated. ^{238}U and therefore ^{226}Ra are naturally abundant in every material. In this thesis we will investigate the possibility to block radon emanation from detector materials to further reduce the background. The usual screening method will be introduced in Chapter 2 and possible coating techniques and materials will be studied in Chapter 3.

[3]Max Planck Institut für Kernphysik, Heidelberg

Chapter 2

On the proportional Counter Detection Efficiency for Radon and its Progenies

In this chapter, a set of ^{222}Rn measurements done with a miniaturized proportional counter will be explained and discussed. The proportional counters were originally designed at the MPIK for the solar neutrino experiment GALLEX [12]. They were intensely used to screen all detector parts of XENON1T for radon emanation, in order to choose materials with the lowest ^{222}Rn emanation [13]. These measurements were done assuming a fixed detection efficiency for radon. This so-called effective counting efficiency for ^{222}Rn was measured to be $(147 \pm 6)\%$ [12], which translates in the detection of about 1.5 α-events for one radon decay. The efficiency is bigger than 1, due to the subsequent α-decays of the radon daughter isotopes, that are also detected. This value is a result of multiple measurements of a ^{222}Rn standard[1] in the past. The aim of this chapter is to determine the counting efficiencies for ^{222}Rn and the α-decays of its daughters ^{218}Po and ^{214}Po. It is already known that the efficiencies are different for ^{222}Rn compared to ^{218}Po and ^{214}Po. This is due to the fact that, the two polonium daughters are mainly positively charged [14] and get affected by the electrical field applied in the proportional counter (see detailed description in Section 2.4.3). In the following, the geometry and the detection principle of the highly sensitive proportional counters will be introduced.

2.1 Detection Principle

The proportional counters are made of quartz glass with a very low radioactive contamination. An image of a proportional counter can be seen in Figure 2.1. The cylindrical counter body contains a similarly shaped cathode made of iron or silicon. A tungsten wire running along the z-axis through the cathode is used as anode. A sketch of the proportional counter can be seen in Figure 2.2. For measurements, a mixture of 90% argon and 10% methane (P10) is used as

[1] A standard is a radioactive sample with a precisely known activity.

counting gas[2] in the approximately 1 cm^3 active volume of the counter.

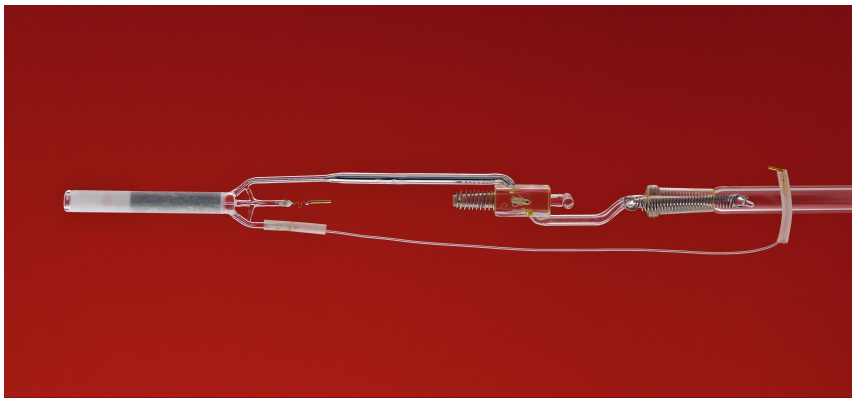

Figure 2.1: Miniaturized proportional counter used for highly sensitive detection of ^{222}Rn decays. The grey part on the left is the active volume of the Counter. It has a total length of around 20cm. Taken from [13].

A particle entering the active volume of the counter can ionize the counting gas. The electrons and ions produced by this ionization are accelerated to the anode and the cathode, respectively, where they are collected. The mean number of ionizations induced by the entering particle (*primary ionization*) is proportional to the energy deposited in the gas. Since there is a high voltage electric field applied to the anode and the cathode, the accelerated electrons can ionize the counting gas again, causing so called *secondary ionizations*. The current induced by these ionizations is amplified and the pulse-shaped signal is stored using its height and time stamp. To measure α-events, a low energy cut is applied to reduce background originating from electronic noise and ambient radiation. Therefore only events with an energy above ~48 keV are taken into account. It is assumed that these events are mostly α-decays from radon and its daughter isotopes. On top of that, since α-decays have a relatively high energy, signals often saturate the amplifier and the exact energy information is lost. The event will still be recorded and since we are only interested in the number of α-events, this does not affect the measurement.

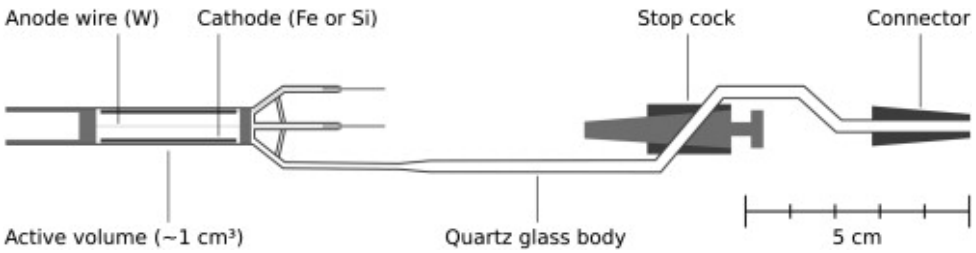

Figure 2.2: Sketch of miniaturized proportional counter, from [15].

[2]The counting gas is mixed with the radioactive sample and filled into the active volume of the counter during the measurement.

2.2 Decay Chain of ^{222}Rn

^{222}Rn is a decay product of the natural radioactive decay chain of ^{238}U, which terminates with the stable element ^{206}Pb. The whole decay chain can be seen in Figure 1.2. It contains α-decays as well as beta-decays. Since the half-life of ^{210}Pb is very long compared to the duration of the measurements, the following α-decay of ^{210}Po is suppressed. When measuring the ^{222}Rn emanation of a sample or of a standard, we have to consider the fact, that the proportional counters detects all α-events coming from ^{222}Rn and its daughter nuclides, with a certain efficiency. For each radon decay, the proportional counter detects more than one α-decay, as already mentioned at the beginning of the chapter.

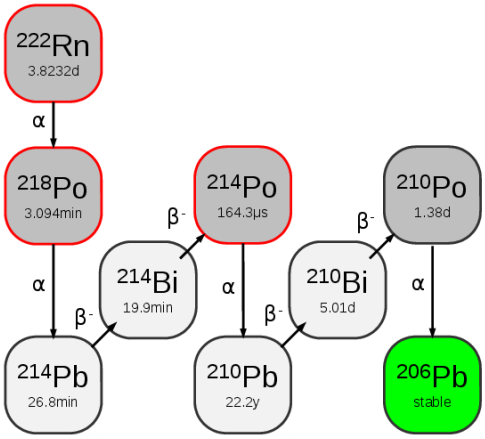

Figure 2.3: ^{218}Rn decay chain. The three detected isotopes decaying by emitting an α-particle are marked in red.

To describe the expected time evolution of the number of events, the decay processes taking place inside the proportional counter have to be understood. At the beginning of each measurement, there are only ^{222}Rn atoms present inside the radon monitor (see Section 2.3). The longer we wait, the more ^{222}Rn will be decayed into its daughter products. Until the decays of ^{222}Rn and its progenies have reached equilibrium[3], the total number of α-events will be described by a growing-in function. The function will be derived in the following. To illustrate the decay of ^{222}Rn, the decay chain starting with ^{222}Rn is shown in Figure 2.3.

Using the radioactive decay law, we can express the processes taking place as a set of differential equations. The decay chain has the form $A \rightarrow B \rightarrow C \rightarrow D \rightarrow E$ (^{222}Rn$\rightarrow$ ^{218}Po$\rightarrow$ ^{214}Pb$\rightarrow$ ^{214}Bi$\rightarrow$ ^{214}Po) with the decay constants λ_a...λ_e. The following equations describe the number of atoms of each element. Equation 2.1 is the radioactive decay law for the radon that is present in the proportional counter at the start of the decay process. The following differential equations 2.2 to 2.3 describe the number of daughter nuclides present inside the proportional counter. The negative part accounts for the decaying atoms, whereas the positive part arises due to the decaying atoms of the mother isotope.

[3] A decay is in equilibrium, when the number of daughter atoms that decay equals the number of atoms that are produced by the decay of the mother atom.

$$\frac{dN_A}{dt} = -\lambda_a N_A \tag{2.1}$$

$$\frac{dN_B}{dt} = -\lambda_b N_B + \lambda_a N_A \tag{2.2}$$

$$\vdots$$

$$\frac{dN_E}{dt} = -\lambda_e N_E + \lambda_d N_D \tag{2.3}$$

Setting the initial values $N_B^0 ... N_E^0$ to zero the system of differential equations can be solved[4] using $N_A(t=0) = N_A^0$. The individual expressions $N_A(t), N_B(t) ... N_E(t)$ are given in Appendix A. Since the proportional counter mainly detects α-events[5], we are only interested in elements A, B and E (referring to ^{222}Rn, ^{218}Po,^{214}Po, respectively). The total event rate is therefore given by:

$$A_{tot}(t, N_A^0) = \lambda_a \cdot N_A(t, N_A^0) + \lambda_b \cdot N_B(t, N_A^0) + \lambda_e \cdot N_E(t, N_A^0) \tag{2.4}$$

Using the solutions given in appendix A and $A_A^0 = A_{Rn}^0$, we get:

$$A_{tot}(t, A_{Rn}^0) = A_{Rn}^0 \cdot e^{-\lambda_a t} + A_{Rn}^0 \left(\frac{\lambda_b}{\lambda_b - \lambda_a} \right) (e^{-\lambda_a t} - e^{-\lambda_b t}) + A_{Rn}^0 \cdot \lambda_b \lambda_c \lambda_d \lambda_e C(t) \tag{2.5}$$

C(t) is a numerical expression given in Appendix A.1. Equation 2.5 can later be used as a fit function to determine the activity of the sample from the measured data. This is done by leaving A_{Rn}^0 as a free fit parameter.

2.3 Measuring Procedure

After deriving the theoretical motivation for the decay processes taking place inside the proportional counter we now explain the measuring procedure performed. The sample used is an aqueous ^{226}Ra solution emanating ^{222}Rn. It can be seen Figure 2.4. The sample was prepared on 19.02.2014 and the ^{222}Rn activity was calculated to be (28.8 ± 0.8) Bq at that time. Before every measurement, the sample was flushed with radon-free helium[6] and afterwards left to emanate for some time. After this emanation time, the sample is extracted and purified. The exact procedure is described in detail in [13]. The extracted radon is mixed with the counting gas and filled into the counter using a dedicated gas-line. As a counting gas, we used P10. After filling, the counter

[4] This was done using Wolfram Mathematica 11.0.

[5] When applying the low energy cut explained in Section 2.1.

[6] Helium is flushed through a cooled, activated charcoal trap to remove radon. More information can be found in [11].

is placed inside a lead shielding to block ambient radiation.

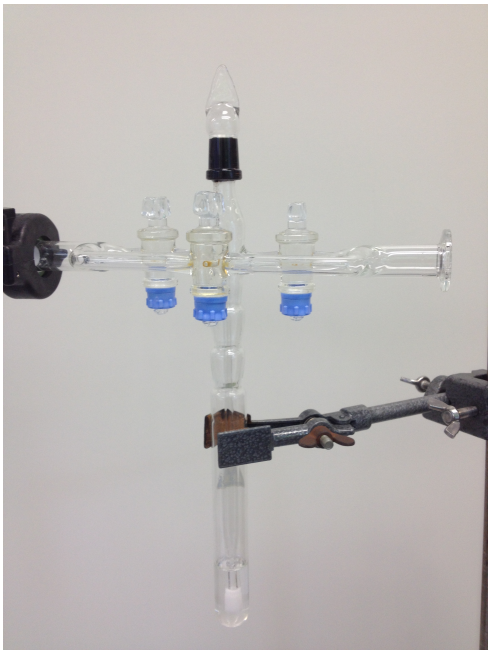

Figure 2.4: ^{226}Rn sample produced on the 19.02.2014 with an activity of 28.8 ± 0.8 Bq.

2.4 Results of the Proportional Counter Measurements

2.4.1 Measurement Overview

The measurement was done twice to gain more statistics. The general information about the measurements can be seen in Table 2.1. Comparing with the low-activity samples that are normally screened using the proportional counters, the amount of events in these measurements is very high. The table shows the total number of events and the number of α-events after applying the low energy cut. The ^{55}Fe calibration source, that will be introduced in Section 2.4.2, was left inside the counter during the measurements. This results in a large increase of the total number events, but it does not contribute to the α-event energy region, since the source has its main emission around 6 keV.

	Emanation time [d]	Duration [h]	Events	α-Events
Measurement 1	1.99 (30.30%)	3.07	316218	100424
Measurement 2	1.02 (16.89%)	2.07	154246	35797

Table 2.1: Measurement overview of ^{222}Rn sample measurements. The number α-events is determined by applying a low energy cut.

2.4.2 Energy Spectrum and Calibration

Figure 2.5 shows the full energy spectrum measured by the proportional counter. It is plotted with a logarithmic scale to get a better idea of its structure.

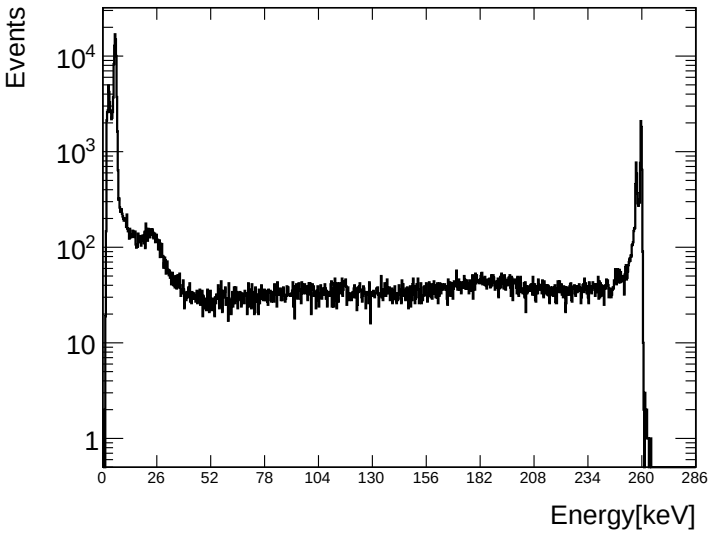

Figure 2.5: Energy spectrum measured by the proportional counter. The calibration was done using the ^{55}Fe peak at 5.95 keV. The data is taken from measurement 2.

At lower energies, the full absorption peak of the calibration source ^{55}Fe is visible. At very high energies we also see an increase in events. This is due to the fact that the proportional counters were not designed to measure α-decays with high energies. Consequently, there is a maximum energy ($\sim$260 keV) that can be detected until the amplifier is saturated.

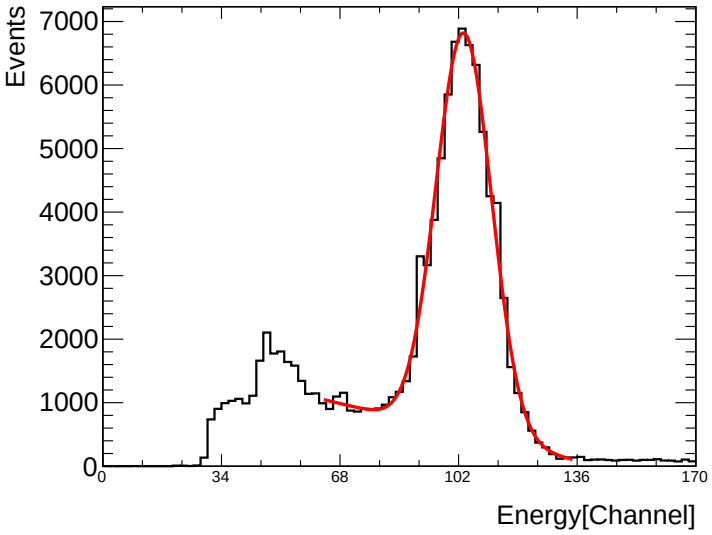

Figure 2.6: The ^{55}Fe full absorption peak is fitted with the superposition of a Gaussian function and a polynomial of first order. The mean value of the Gaussian is assumed to be at 5.95 keV to calibrate the energy spectrum, assuming a linear scale.

Generally, the events are detected and stored in so-called *channels*. They are sorted into the channels depending on their energy. After calibration, the channels can be correlated to energies. This is the reason why we need a calibration source with a well known energy. In our case we use

the ^{55}Fe x-ray source as will be explained in the following. If an energy exceeds the maximum energy, it is recorded in the last channel, the *overflow* channel. As a result of the DAQ, the content of this channel is spread across a set of channels. The peak at $\sim 26\,\text{keV}$ and the bump at $\sim 200\,\text{keV}$ will be investigated in section 2.4.3.

The energy calibration is done using a ^{55}Fe source. For this measurement the source is placed next to the counter inside the lead shielding and is left there for the duration of the measurement. This was done to monitor the stability of the DAQ, by checking the constant event rate of the calibration source. The calibration is done by fitting this peak with the superposition of a polynomial of first order and a Gaussian function. The fitted peak can be seen in Figure 2.6. The polynomial of first order describes the background contribution, while the Gaussian function accounts for the decay energies. The energy scale of the proportional counter is assumed to be linear and the peak position of the calibration source is taken to be at 5.95 keV. Both were shown in [13], even though the linearity was only confirmed for energies lower than $\sim 39\,\text{keV}$. Since we count all events with an energy higher than $\sim 48\,\text{keV}$, the energy scale does not have to be linear at higher energies.

2.4.3 Peak Analysis

Two peaks have been fitted, as shown in Figure 2.7. The first peak was fitted with the superposition of a Gaussian function and a polynomial function of first order. The second peak was fitted with the superposition of a Gaussian function and a constant.

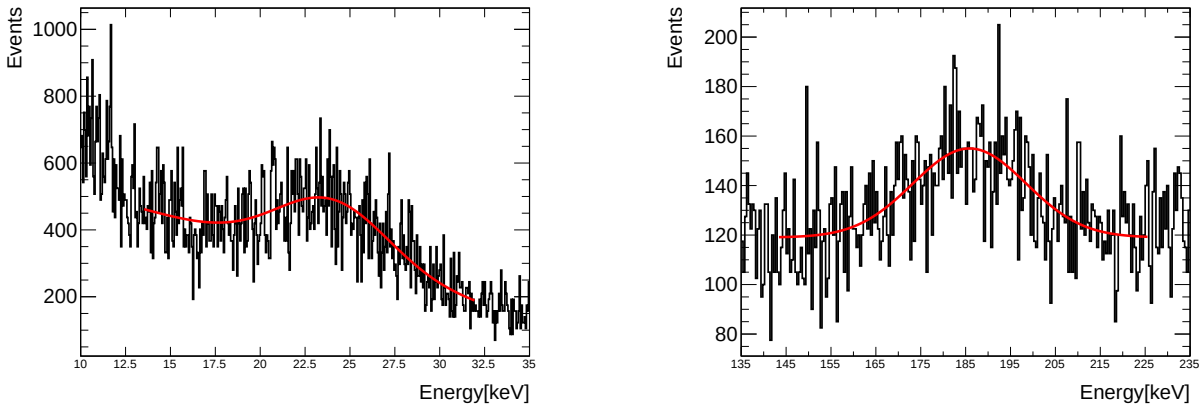

(a) Peak 1. **(b)** Peak 2.

Figure 2.7: Fitted peaks in the energy spectrum measured with a proportional counter (see Figure 2.5).

The mean values of the Gaussian functions determined by the fits can be seen in Table 2.2. This is used as the energy position of the peaks. It can be seen that there is a good agreement in both measurements for the first peak. The position of the second peak, on the other hand, differs substantially, although we have to bear in mind that the energy scale of the proportional counter

might not be linear at these energies and we did not take into account any systematic errors.

Generally, we know that events with energies lower than ∼48 keV come from β-decays and γ-particle interactions. The first peak must therefore originate from one of the processes that could be associated to the daughter isotopes of ^{222}Rn (see Figure 2.3). There are many different secondary events happening in addition to the α-events of ^{222}Rn, ^{218}Po and ^{214}Po. One possible explanation for this energy peak is the energy deposited by electrons emitted from internal conversion happening in the excited ^{214}Bi isotope [16].

	Peak 1 [keV]	Peak 2 [keV]
Measurement 1	24.4 ± 0.1	179 ± 1
Measurement 2	24.0 ± 0.3	186 ± 1

Table 2.2: Mean values of the two peaks observed in the energy spectrum shown in Figure 2.5. They were determined using a Gaussian fit.

The second peak is at high energy and can not be explained by β-decays or γ-particle interactions. The events in this peak must be α-events because of the high energy, but since the entire decay energy of an α-particle is in the order of a few MeV, there should not be a peak in this region. A possible cause could be the effect of *plate out* that was shortly mentioned at the beginning of this chapter. The positively charged radon progenies ^{218}Po and ^{214}Po [14] are collected at the cylindrical cathode whereas ^{222}Rn is distributed homogeneously in the active volume of the proportional counter. This might have an effect on the detection efficiency of the α-particle from the polonium decays. The time evolution of the number of counts in the second peak was analysed to find an indication supporting this hypotheses[7]. Since there was no conclusive result, the origin of the second peak is not known yet and has to be further studied.

2.4.4 Detection Efficiency Results for ^{222}Rn, ^{218}Po and ^{214}Po

In order to determine the detection efficiencies of the three α-decays measured in the proportional counters, the function derived in Section 2.2 was used to fit the data. If the detection efficiency for all the α-decays was 100%, this would be a way to determine the equilibrium activity A of the sample. However, since this is not the case, we determine the detection efficiencies times the equilibrium activity ($\epsilon_i \cdot A$) for every isotope (i∈{222,218,214}). In Figure 2.8 the time evolution of the second measurement including the fit can be seen.

The fit results are listed in Table 2.3. The statistical error was determined by the fit with ROOT, whereas the systematic error was estimated varying the decay start time. This is the exact time, when the ^{222}Rn sample started decaying in the counter. This time is not known to the second, therefore we approximated a systematic error by varying it by ± 30 s, and fitting data again. The change of the fit parameters, with regard to the fit parameters found using the correct decay

[7] At the beginning there are comparatively more radon decays since the polonium decays have not grown into equilibrium.

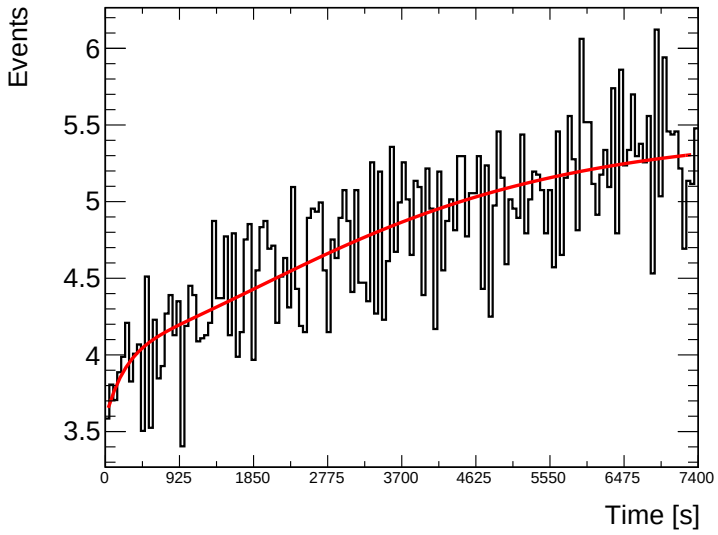

Figure 2.8: Time evolution of detected α-events fitted using the function derived in Section 2.2. There are three fit parameters, representing the individual detection efficiency times the activity of the sample, labelled as "$\epsilon_i \cdot A$" in Table 2.5. Data taken from measurement 2.

start time, is used to estimate the systematic error.

	Measurement 1 [Bq]	Measurement 2 [Bq]
$\epsilon_{222} \cdot A$	$15.99 \pm 1.17_{stat} \pm 0.89_{sys}$	$16.00 \pm 1.80_{stat} \pm 0.84_{sys}$
$\epsilon_{218} \cdot A$	$8.94 \pm 1.20_{stat} \pm 0.84_{sys}$	$8.43 \pm 1.90_{stat} \pm 0.78_{sys}$
$\epsilon_{214} \cdot A$	$8.42 \pm 0.30_{stat} \pm 0.05_{sys}$	$8.75 \pm 0.55_{stat} \pm 0.05_{sys}$

Table 2.3: Activity measurement results of ^{222}Rn sample measurements.

The results from the two measurements are in very good agreement. To evaluate the detection efficiencies of the proportional counter for each isotope, we consider the total measured activity: $A_{tot} = \epsilon_{222} \cdot A + \epsilon_{218} \cdot A + \epsilon_{214} \cdot A$. This results in $A_{tot}^{M1} = (33.35 \pm 2.92)\,\text{Bq}$ and $A_{tot}^{M2} = (33.18 \pm 3.81)\,\text{Bq}$. Now, we can calculate the ratio of the activity, measured for each isotope to the total measured activity and compare them between each other. This is done in Table 2.4.

	Measurement 1	Measurement 2	Average
$(\epsilon_{222} \cdot A)/A_{tot}$	0.48 ± 0.04	0.48 ± 0.06	0.48 ± 0.04
$(\epsilon_{218} \cdot A)/A_{tot}$	0.27 ± 0.05	0.25 ± 0.06	0.26 ± 0.04
$(\epsilon_{214} \cdot A)/A_{tot}$	0.25 ± 0.02	0.27 ± 0.03	0.26 ± 0.02

Table 2.4: Activity ratios of individual isotope activity to total activity.

Using the effective detection efficiency of the proportional counters $E_{eff} = (0.147 \pm 0.006)$ [12], we can calculate the detection efficiency for each α-decay by multiplying the values from Table 2.4 with the effective efficiency:

$$\frac{\epsilon_i \cdot A}{A_{tot}} \cdot E_{eff} = \epsilon_i \tag{2.6}$$

where A_{tot} is the total measured activity and A is the activity of the sample. The effective detection efficiency of the proportional counters is defined as: $E_{eff} = A_{tot}/A$. The final result can be seen in Table 2.5.

α-decay	Efficiency ϵ [%]
^{222}Rn	70 ± 7
^{218}Po	38 ± 6
^{214}Po	38 ± 5

Table 2.5: Detection efficiency of the proportional counters for ^{222}Rn, ^{218}Po and ^{214}Po.

This means that 70% of all ^{222}Rn α-decays and 38% of all the ^{218}Po and ^{214}Po α-decays are detected in the proportional counter. One reason why the detection efficiency for all decays is reduced is because every proportional counter has a dead volume, where no α-decays are measured. Generally, the dead volume of a counter amounts to 10%-15% [17]. The reason why the detection efficiency for ^{222}Rn is significantly higher than for the two polonium daughters is the effect of *plate out*, that was already mentioned before. The mainly positively charged polonium isotopes get accumulated at the cylindrical cathode and are not distributed homogeneously inside the counter any more. Sitting at the outside of the active volume of the counter, the chance, that the polonium α-particles leave the counter is higher than for the homogeneously distributed radon atoms. As a result, fewer polonium decays are detected. Since this is the case for both ^{218}Po and ^{214}Po, they have the same detection efficiency. The results in Table 2.5 confirm this. The detection efficiency for ^{222}Rn is too low to be explained only be the dead volume of the counter. Consequently, there must be other effects effecting the detection efficiency. In this study, there was no conclusive result as to the origin of these effects. This matter therefore has to be further studied.

Chapter 3

Reducing the Emanation of Radon by applying Material Coatings

The general idea of coating is that a layer of a radio-pure material on the surface of a contaminated material should prevent radon emanation. There are two main reasons why radon emanates in the first place. The first reason is that the mother isotope of radon are in solid form, but radon itself is gaseous and can therefore diffuse out of the material, if the mother nuclide was close to the surface. The other reason is the effect of nuclear-recoil. An isotope is recoiled as a result of the radioactive α-decay[1] of its mother nuclide. If the mother nucleus is close to the surface, this recoil energy can be enough to transport it out of the material.

The coated layer thus needs to fulfil two tasks. It has to be tight to stop radon from diffusing and it has to be thick enough to prevent recoil. Generally, the material used for coating could be any radio-pure metal. However, copper is thought to be a good candidate, since high-purity copper is already commercially available, and, in many cases, copper also meets the desired thermal, mechanical or electrical properties. Titanium is tested as a second material for coating. Its radio-purity and mechanical strength also fit the criteria of a possible good coating material.

3.1 Radon Monitor

To investigate if coating a surface could block radon emanation we need a fast and reliable way to determine the emanation of a sample. One possible approach is the detection using the proportional counters introduced in chapter 2. However, these highly sensitive radon measurements are not designed for a continuous detection of comparatively high activities and furthermore cannot discriminate between distinct α-decays. Instead we use the radon monitor shown in Figure 3.1a. Here, the radioactive decays are detected using a Si pin diode (see Figure 3.1b). The detection principle will be explained in more detail in the next Section.

[1] An α-decay is the emission of an α-particle (helium nucleus).

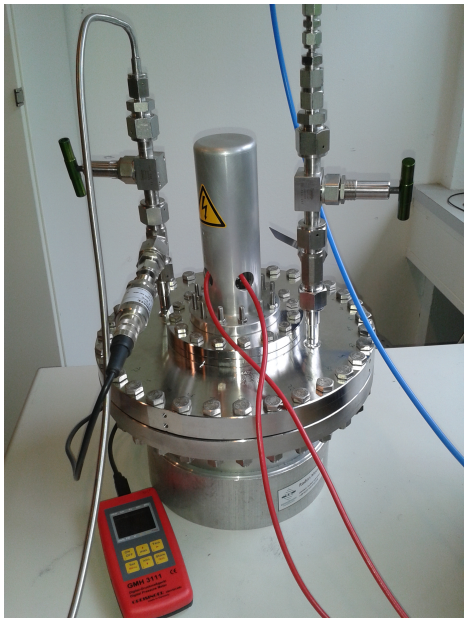

(a) Radon Monitor with a volume of ∼4 l. The metal pipe can be connected to a vacuum pump, whereas the blue one is connected to a Nitrogen supply. The pressure sensor with its readout can also be seen.

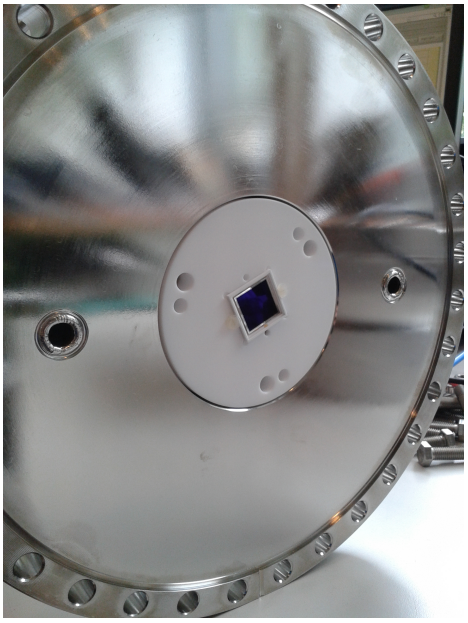

(b) Si pin diode embedded in top flange of radon monitor. The diode is framed by a Teflon insulator (white disc).

Figure 3.1: Radon monitor setup and Si pin diode.

3.1.1 Detection Principle

The radon monitor is a semiconductor detector. The α-decays are detected using a Si pin diode. Since most progenies created by an α-decay are positively charged [14], a negative high voltage of -1000 V is applied to the Si pin diode to create an electric field that drifts them towards the diode. Once they are on the pin diode, their decay can be measured, since the α-energy is deposited directly into the diode. The pin diode contains a semiconductor material connected to two electrodes. The material is doped with silicon in order to increase the width of the depletion region and the diode is reversely biased. If an isotope decays on the pin diode it deposits energy and produces electron-hole pairs. Because the diode is reversely biased this causes a small current with opposite sign in anode and cathode. This current is amplified and measured and the energy of the decay can be obtained since the generated ionization charge is proportional to the deposited energy of the radioactive decay. Of course this is only correct if the whole energy of the decay was absorbed. Figure 3.2 shows the signals recorded by an oscilloscope for an α-decay.

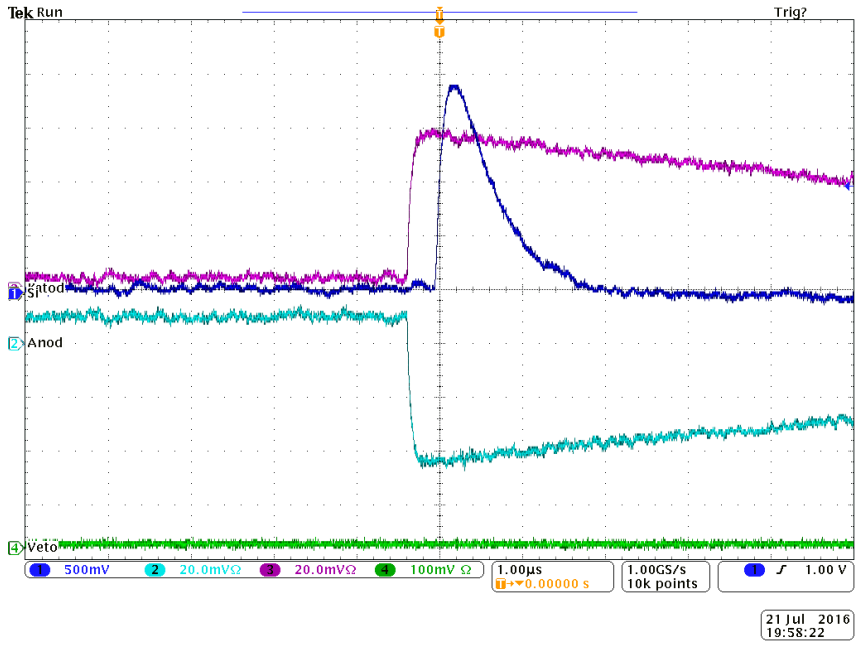

Figure 3.2: The signal from anode and cathode can be seen in purple and turquoise. The blue signal is the summed signal of the two, after amplification. Its height is proportional to the energy of the decay

3.2 Coating Techniques

Two different techniques and materials were used to study the effect of surface coating on the emanation of radon. The first coating technique is called plasma coating[2]. It was used in combination with copper as a coating material. The technique utilises an arc-heated plasma jet to deposit different raw materials on a surface. In the plasma generator an electric arc is created by a strong current. This arc heats up gas flowing through the generator, resulting in a plasma jet of several thousand degrees [18]. The raw material, which is copper in our case, is directly mixed into the plasma jet in any state. Most of the time, the plasma coating is performed in vacuum to reduce the effect of air. The thicknesses of the coated, copper layer were estimated to be around 1 μm. This was done by Dr. Laure Plasmatechnologie, by weighing the samples before and after coating.

The second coating technique is a form of physical vapour deposition (PVD) called spluttering[3]. The target material, which is titanium in our case, is vaporised by bombardment with laser beams, ions, or electrons [19]. The vaporised material moves through a vacuum chamber and condenses onto the samples to be coated, forming a layer. The movement through the vacuum is sometimes lead by an electric field. The thickness of the titanium layer, achieved by this technique, was estimated to be 400 nm at the edges and 800 nm at the middle of the sample.

[2]Done by Dr. Laure Plasmatechnologie GmbH, Stuttgart.
[3]Done by EC Europ Coating GmbH, Dresden.

3.3 Experimental Setup and Samples

A sketch of the experimental setup used to determine the emanation of the samples is shown in Figure 3.3. The central part is the radon monitor. Additionally, there is a pressure sensor, a gas inlet for nitrogen and a port to connect a vacuum pump. The samples that were used for these measurements are thoriated tungsten electrodes (welding rods). They contain ∼4% of ^{232}Th and thus emanate ^{220}Rn. Even though the main background in XENON1T comes from ^{222}Rn [10], some first tests on a ^{220}Rn sample could prove helpful to confirm the effect of coating. The decay chain and detection of ^{220}Rn will be discussed in Section 3.3.1. The samples are 175 mm long rods of 1 mm diameter. For the measurements, the samples were directly placed inside the radon monitor as can be seen in Figure 3.4b.

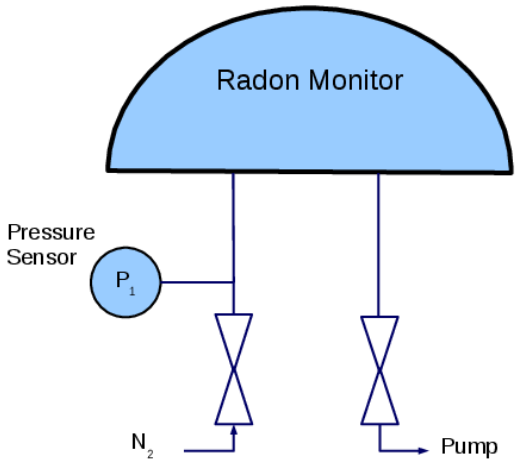

Figure 3.3: Setup used for ^{220}Rn Measurements.

Several sets of welding rods were measured and afterwards coated with copper and titanium using different coating techniques that will be explained in Section 3.2. They were then measured again to investigate the effect of the coatings.

At the beginning of each measurement, the top flange of the radon monitor was taken off (see Figure 3.1b), and a certain number of rods were placed directly inside the radon monitor (see Figure 3.4b). Then the flange was placed back on top and, for measurements done in air, the data acquisition was started immediately. For measurements done in N_2, the flange was closed while the radon monitor was flushed with nitrogen. Once sealed, it was filled with nitrogen and then pumped to vacuum. Then, it was again filled with N_2 to around 1050 mbar and the valves were closed. Then a high voltage of -1000 V was applied and the data taking was started. After a few days the same procedure is repeated. In between the measurements, a *blank* measurement was done. This does not indicate a background measurement of the radon monitor, but rather the detection of the decaying ^{220}Rn progenies that were collected inside. As will be shown in Section 3.4.1, this allows us to do an energy calibration and monitor the residual background for consecutive measurements.

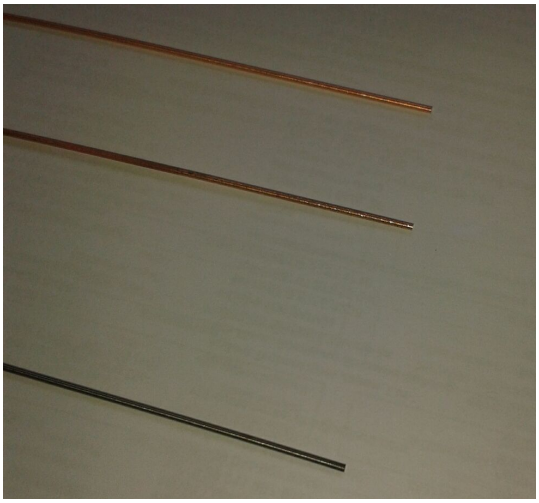

(a) The top two rods were coated with copper. The bottom one is in its original form without a coating.

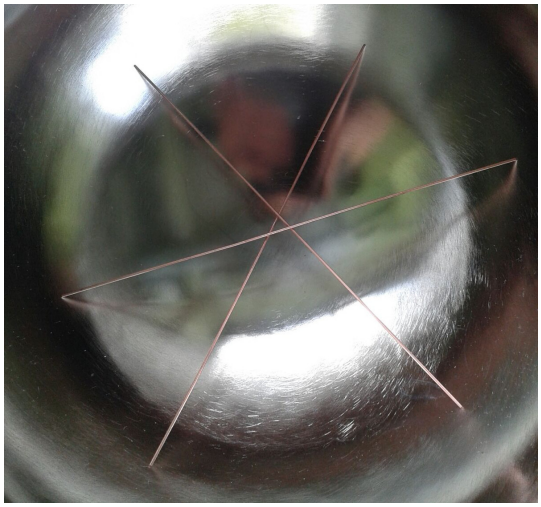

(b) Copper coated welding rod samples inside the radon monitor.

Figure 3.4: Welding rod samples.

3.3.1 Detection of ^{220}Rn in the Radon Monitor

After the sample was placed inside the radon monitor, the ^{220}Rn emanation starts. The gaseous ^{220}Rn distributes inside the radon monitor, where it decays. Its daughter isotopes, that are mainly positively charged, shown here [14] for ^{218}Po, are collected and their decays can be detected. The detailed detection principle will be explained in Section 3.1.1. As will be explained, the detection efficiency is highest for ^{212}Po. It also has the highest decay energy with $E_{^{212}Po}$=8.954 MeV [8]. Since the radon monitor allows an energy discrimination between different α-events (explained in Section 3.1.1), it is easy to identify the ^{212}Po decay peak.

In order to describe the ^{212}Po activity evolution during a measurement we have to discuss the decay process taking place in the radon monitor. At the beginning of each measurement, there are only ^{220}Rn atoms present inside the radon monitor. Using the radioactive decay law, we can express the processes taking place in a set of differential equations (compare with Section 2.2). This time it has the form $A \rightarrow B \rightarrow C \rightarrow D$ (^{216}Po$\rightarrow^{212}$Pb$\rightarrow^{212}$Bi$\rightarrow^{212}$Po) with the decay constants $\lambda_a ... \lambda_d$. We start with ^{216}Po instead of ^{220}Rn, because its half-life is very short with $T_{1/2}^{216Po} = 0.14\,\mathrm{s}$ [8], and we can therefore assume it is already in equilibrium at the beginning. Using the same set of differential equations 2.1, 2.2 to 2.3 we can find the solutions, choosing the correct initial conditions. Since the rods contain the long lived ^{232}Th, there is a constant amount of ^{216}Po present in the detector. We can therefore choose our initial conditions to be: $N_B^0 = 0, N_C^0 = 0, N_D^0 = 0$ and $N_A(t) = const = N_A^0$. The function that will be used to fit the time evolution of the number of events in the ^{212}Po peak will be:

$$A_{212Po}(t, N_A^0) = \lambda_{212Po} \cdot N_D(t, N_A^0) \tag{3.1}$$

where $N_D(t, N_A^0) = N_{212Po}(t, N_A^0)$. Using $N_A = const = N_A^0$ as a free fit parameter allows us to determine the activity of the sample. The exact solution for $N_D(t, N_A^0)$ can be found in Appendix B.1.

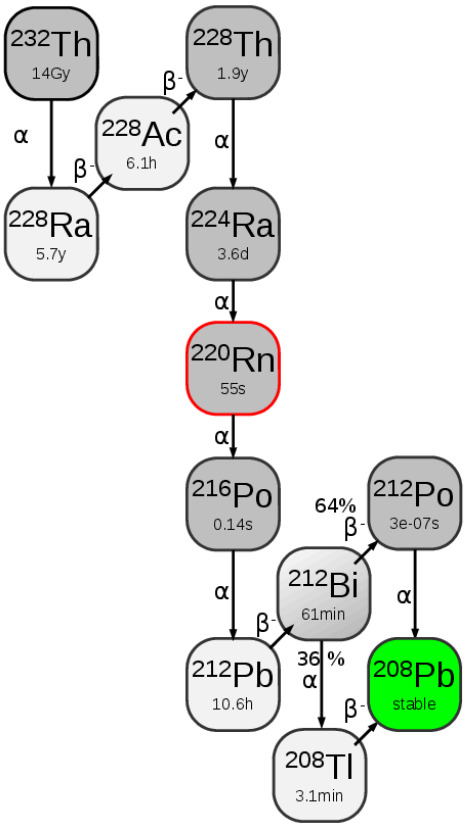

Figure 3.5: ^{232}Th decay chain. The isotope ^{220}Rn that we want to measure is marked in red.

For the blank measurements done in between the measurements, a similar approach can be used to describe the decay processes taking place. At the start of these measurements the decay of ^{212}Po had reached equilibrium, so we can use a similar set of differential equations as before to describe what happens if we remove the constant production of ^{216}Po. The ^{216}Po progenies will decay obeying the solution of the differential equations if we set the initial conditions right. This time the decay has the form $A \to B \to C$ (^{212}Pb$\to^{212}$Bi$\to^{212}$Po) with corresponding decay constants. The initial conditions are chosen to be $A_A^0 = \lambda_a \cdot N_A^0 = A_B^0 = \lambda_b \cdot N_B^0 = A_C^0 = \lambda_c \cdot N_C^0$, since they are in equilibrium. The exact solutions can be found in Appendix B.1. The function used to describe the data will be:

$$A_{212Po}(t, \lambda_{212Po}) = \lambda_{212Po} N_C(t) \tag{3.2}$$

Where $N_C(t) = N_{212Po}(t)$. In this case not the activity A_{212Po}^0 but instead the decay constant λ_{212Po} will be used as a free fit parameter, to confirm that the identified peak is the ^{212}Po peak.

3.4 Results of the Radon Monitor Measurements

3.4.1 Energy spectrum and calibration

Figure 3.6 shows the typical energy spectrum of a thoriated, tungsten welding rod sample, detected by the radon monitor. There are distinct peaks from the α-decays happening within the ^{232}Th decay chain. As a first step, we want to identify the peaks and do an energy calibration. This is done by taking the position of the energetically highest peak (Peak 6) and assigning its position to $E_{^{212}Po}$=8.954 MeV [8]. Using the half-live of ^{212}Po as a free fit parameter, we can fit an exponential decay[4] to the time evolution of the number of events in this peak, to confirm its origin. The average half-life estimated from the measurements of the first sample is ${}^{exp}T_{1/2}^{212Po} = (3.1 \pm 0.2) \cdot 10^{-7}$ s. The theoretical half-life of ^{212}Po is ${}^{theo}T_{1/2}^{212Po} = 3 \cdot 10^{-7}$ s. Therefore we identified Peak 6 correctly as the decay peak of ^{212}Po.

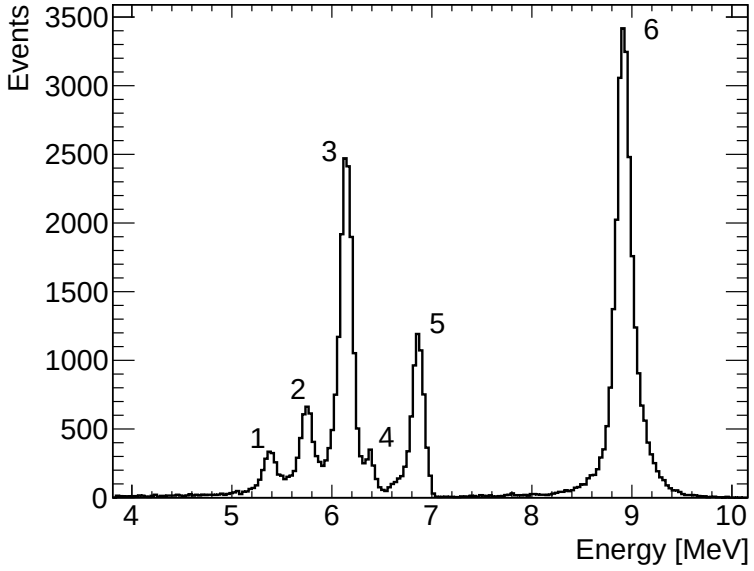

Figure 3.6: α-energy spectrum of the radon monitor measurement of welding rod Sample 2 Measurement 1 (see Table 3.3). This measurement was done in nitrogen. Peak 6 was identified as ^{212}Po peak and used for Calibration. The other peaks are identified by their energy as shown in Table 3.1.

In order to identify the other peaks, we estimate their position as the mean value of a Gaussian fit. The observed non-Gaussian tailing will be discussed later in this section. Using the ^{212}Po peak (Peak 6) as a reference, we can identify the other peaks with the α-decays in the ^{220}Rn decay chain by their energies. The determined α-decay energies of the peaks matched with the literature values are shown in Table 3.1.

Peak 1 can be identified as the ^{210}Po peak. Looking at Figure 2.3 we see that ^{210}Pb has a half-life of $T_{1/2}^{210Pb} = 22.2$ y [9]. Therefore there is a constant production and decay of ^{210}Po which has been collected at the diode in previous measurements.

Peak 2 is originating from the decay of ^{224}Ra. When ^{228}Th decays, the ^{224}Ra atom is recoiled. Due to the recoil the atom is transported out of the material into the radon monitor. As it is

[4] We use the function derived in Section 3.3.1

Peak	Experimental Values [MeV]	Literature Values [MeV]
P1(^{210}Po)	5.385 ± 0.084	5.407
P2(^{224}Ra)	5.751 ± 0.073	5.789
P3(^{212}Bi)	6.137 ± 0.069	6.207
P4(^{220}Rn)	6.379 ± 0.039	6.405
P5(^{216}Po)	6.858 ± 0.061	6.906
P6(^{212}Po)	-	8.954

Table 3.1: Peak Positions of Sample 2 Measurement 1 (see Table 3.3), determined by a Gaussian Fit. The error of the experimental values is one standard deviation, derived by the Gaussian fit. Theoretical values are taken from [8] and [9].

positively charged, it is collected at the Si pin diode and the decay can be detected.

Peak 4 is matched with the decay of ^{220}Rn, that is produced as a daughter isotope in the ^{224}Ra decay. Generally, the detection efficiency should increase for isotopes later in the decay chain. This is the case because the atoms drift to the diode and stay there. As a result the daughter isotopes are already at the diode where they can be detected. The atoms that are not at the diode are again drifted towards it. Quite contrary, the height of Peak 4 is smaller than the height of Peak 2. This can be explained by the diffusive effect of radon that was describe at the beginning of Chapter 3. The ^{220}Rn isotopes produced by the decay of ^{224}Ra are in gaseous state. The half-life of ^{220}Rn ($T_{1/2}^{220Rn} = 56\,\mathrm{s}$ [8]) is long enough for the ^{220}Rn to diffuse away from the diode. As a result, their decay cannot be detected any more. This in only true for some of the ^{220}Rn atoms, since many decay fast enough to be detected.

Peak 5 can be identified with the decay of ^{216}Po. This peak is significantly higher than Peak 4. The positively charged daughter isotope ^{216}Po of the ^{220}Rn decay is again collected at the diode and the decay can be detected.

Peak 3 originates from the ^{212}Bi α-decays. As we can see in Figure 3.5, this decay occurs with a branching ratio of 36%. The ^{212}Po decay on the other hand occurs with a branching ratio of 64%. Looking at the ratio of the number of events in each peak and the total number of events in both peaks we find: $\frac{N_3}{N_3+N_6} = (34 \pm 3)\%$ and $\frac{N_6}{N_3+N_6} = (66 \pm 3)\%$. The error is due to the fact that we did not take into account the number of events in the tail of Peak 2.

For comparison, Figure 3.7 shows the energy spectrum measured in ambient air instead of nitrogen. Since air contains a small amount of ^{222}Rn, we expect to see additional peaks from its progenies (see Figure 2.3). Looking at Figure 3.7 we can clearly find the ^{214}Po Peak with an energy of $E_{214Po}^{exp} = (7.79 \pm 0.06)\,\mathrm{MeV}$ ($E_{214Po}^{lit} = (7.833)\,\mathrm{MeV}$ [9]). The ^{218}Po Peak is also visible, but overlapped with the ^{212}Bi Peak, therefore we cannot quantify its energy. But comparing with the theoretical value $E_{218Po}^{lit} = 6.11\,\mathrm{MeV}$[9], it is at the right position. We noticed that there is no overlap of any peaks with ^{212}Po peak, which will later be used for analysis.

Peak 5 shows the typical shape of an α-decay. It has a sharp cut-off towards higher energies, because there is a maximum energy that can be deposited. This is not the case for Peak 6.

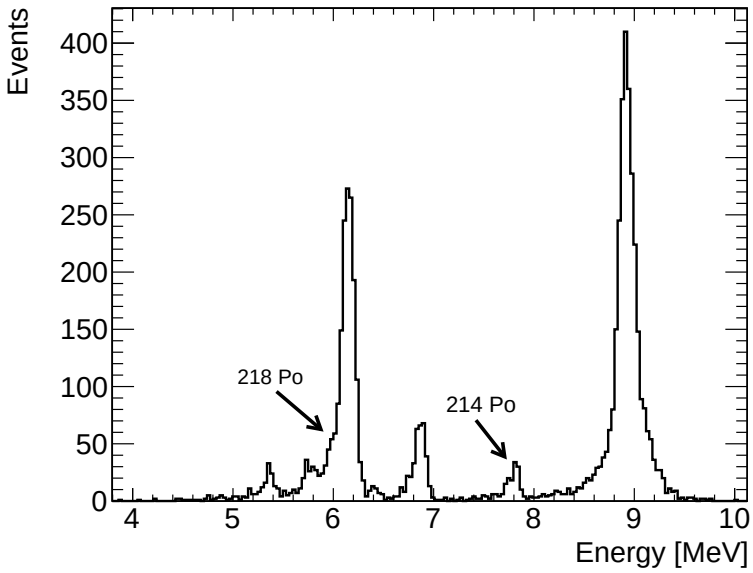

Figure 3.7: α-energy spectrum of the radon monitor measurement of welding rod Sample 1 Measurement 1 (see Table 3.3). The measurement was done in air.

Looking at the decay scheme in Figure 3.5, we can explain the peak shape of the ^{212}Po peak by its very short half-life of $T_{1/2}^{212Po} = 3 \cdot 10^{-7}$ s. A a consequence the ^{212}Bi β-decay and the ^{212}Po decay happen simultaneously in most of the cases. Therefore, the energy depositions of both decays are detected at once. As a result, energies higher than the α-energy of the ^{212}Po decay can be measured.

3.4.2 Systematic Effects of the Radon Monitor

Linearity

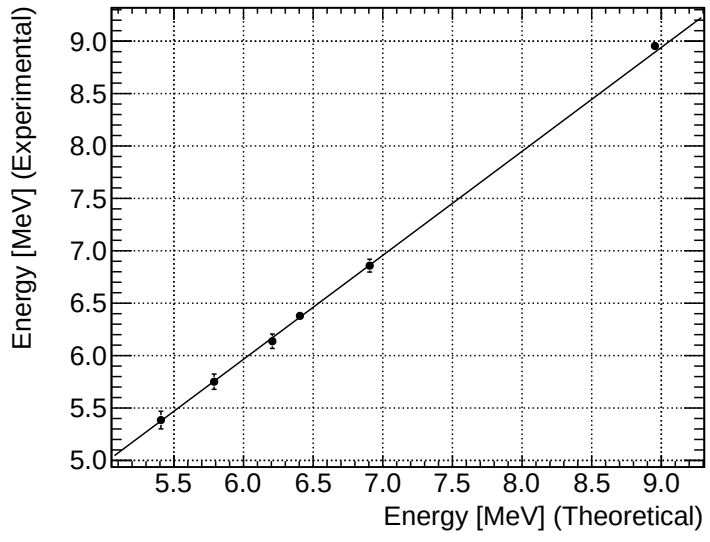

Figure 3.8: The peak positions from table 3.1 were plotted and fitted linearly to estimate the linearity of the radon monitor. The error of the experimental values is one standard deviation, derived by the Gaussian fit.

Using the peak positions from table 3.1, we can estimate the linearity of the radon monitor. We plot the experimental values, using one standard deviation of the Gaussian function as error, against the theoretical values, and apply a linear fit. The result can be seen in Figure 3.8 with the following fit parameters: $P_0 = (-0.014 \pm 0.384)\,\text{MeV}$ and $P_1 = 0.992 \pm 0.06$ with $\chi^2/ndf = 0.355/3$. This shows that the energy scale of the radon monitor is linear, although the small χ^2 value tells us that we overestimated the errors of the peak positions.

Effect of Humidity

An additional measurement was done to investigate the effect of humidity on the detection efficiency of the radon monitor. For this purpose the measurement of a known sample was repeated, while the humidity was artificially increased, by placing a small bowl of water inside the radon monitor. The measurement was done in air. The activity values of the measurement with and without increased humidity are in agreement, as can be seen in Table 3.2. The effect of the humidity on the detection efficiency is therefore assumed to be negligible for our measurements.

	Ingrowth [mBq]	Counts/Time [mBq]
Normal Measurement	13.8 ± 1.2	13.8 ± 0.4
Increased Humidity	15.2 ± 0.8	15.2 ± 0.3

Table 3.2: Activity values measured with and without increased humidity.

3.4.3 Activity Measurements Before Coating

As stated before we only use the most dominant peak of the ^{212}Po α-decay. Using the function derived in Section 3.3.1, we can fit the time evolution of number of events in the peak and thereby obtain the activity of the sample. The results of this method will be denoted with *Ingrowth* in the following. In Figure 3.9 the time evolution and the fit are shown for one of the measurements.

	Measurement	Ingrowth [mBq]	Counts/Time [mBq]
Sample 1	1	46.8 ± 2.0	44.3 ± 0.7
(6 rods)	2	54.6 ± 0.5	54.5 ± 0.5
	3	41.1 ± 0.4	41.4 ± 0.4
Sample 2	1	39.1 ± 0.3	38.9 ± 0.2
(6 rods)	2	40.4 ± 0.3	40.3 ± 0.4
Sample 2 A	1	21.3 ± 0.3	20.8 ± 0.3
(3 rods)	2	21.4 ± 0.3	21.4 ± 0.2

Table 3.3: Coating measurement results. Sample 2 A is half of Sample 2.

In addition to that, we use a complementary analysis. We can take the number of decays in a certain interval of time and the ratio gives us the activity (Denoted as *Counts/Time* from now on). In case we did not fully reach equilibrium, we have to correct the activity using the ingrowth

function derived in 3.3.1. With these two analysis methods we get two activity values for each measurement. The results for the welding rods before coating can be seen in Table 3.3.

Sample 1 & 2 are six identical welding electrodes. Sample 2 A is a sub-sample of Sample 2 containing three electrodes. Measurement 1 of Sample 1 was done in air. Measurement 2 and 3 of Sample 1 were done in nitrogen. We observed a leak for measurement 2. The measurements for Sample 2 and Sample 2 A were entirely done in nitrogen.

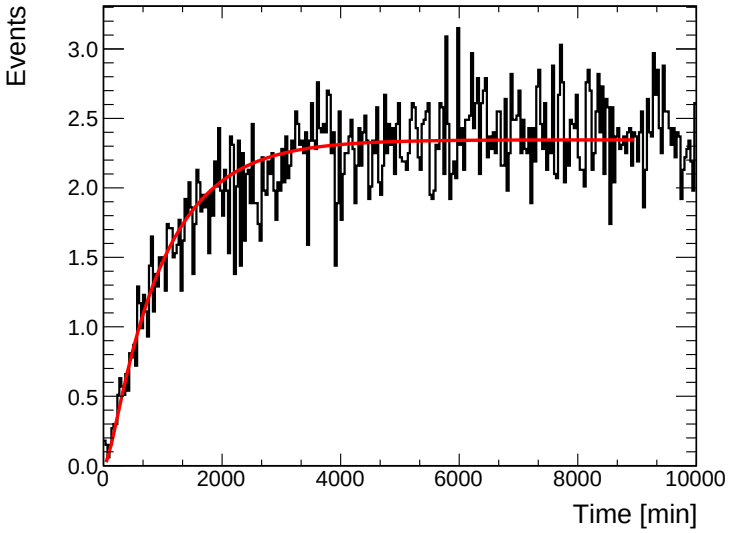

Figure 3.9: The time evolution of the ^{212}Po peak is fitted using the function derived in Section 3.3.1. The only fit parameter is the ^{212}Po equilibrium activity denoted as "Ingrowth" in table 3.3. $\chi^2/ndf = 9/269$. The data is from Sample 2 Measurement 1.

The determination of the absolute activity of the samples is difficult without knowing the detection efficiencies of the radon monitor. We make an estimation on the efficiency of the radon monitor for ^{212}Po, by using the geometry of the pin diode. We can argue, that only half of the α particles from the decay are detected. The reason is, that an α-particle being emitted by an atom sitting on a planar surface has a 50% chance to fly away from the surface. In this case it will not be detected by the radon monitor. On top of that, looking at Figure 3.5, we know that, of all the ^{220}Rn isotopes decaying, only 64% will decay through the ^{212}Po chain. Therefore we can set a maximum value for the efficiency to be: $E_{max}^{212Po} = 0.64 \cdot 0.50 = 0.32 = 32\%$. Using the average value of all measurements for Sample 1 from table 3.3 and corrected with the efficiency we get and activity of $A_{220Rn} = \dfrac{7.85\text{mBq}}{0.32} = 24.53\,\text{mBq}$ per electrode.

3.4.4 Activity Measurements After Coating

Copper Coated Sample

After the welding electrodes were coated with copper, they were examined using a scanning electron microscope to ensure that they were coated entirely. Apart from a few small spots where the tungsten still shines through, the whole electrodes were coated. The images can be found in Appendix C. Using an optical microscope the surface structure of the coated and

uncoated electrodes was observed as shown in Figure 3.10. The coated copper layer is not as smooth as the original welding electrode. At some places there are solidified drops of copper visible.

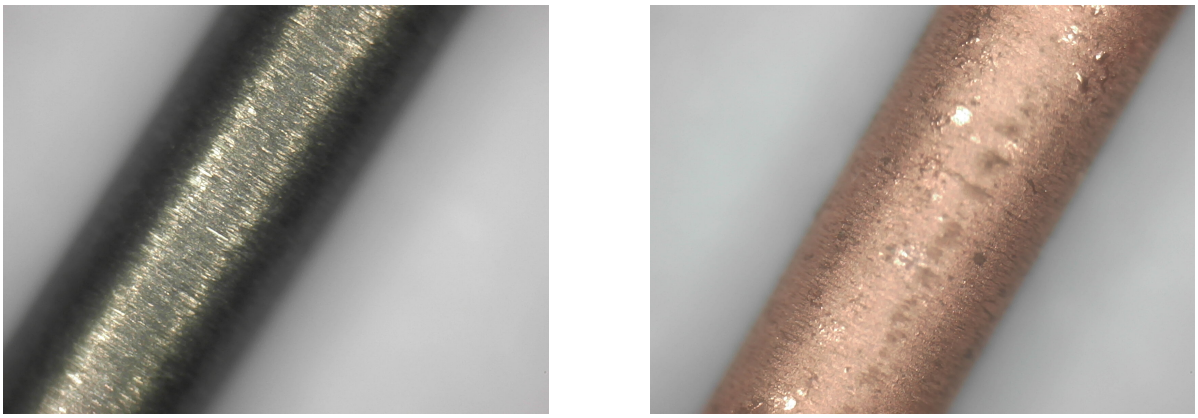

(a) Before Coating. **(b)** After Coating.

Figure 3.10: Microscope images of WTh(4%) welding electrodes before and after coating with copper.

The measurements done in Section 3.4.3 were repeated for the copper coated welding electrode samples. Before coating we measured six welding electrodes named Sample 1 (see Table 3.3). Three of theses six were entirely coated with copper (Sample 1 A). The other three were only partly ($\sim 65\%$) coated with copper (Sample 1 B). The emanation results are shown in table 3.4. The Measurement 1 of Sample 1 A was done in nitrogen, whereas Measurement 2 was done in air. We observed a leak for Measurement 1. The Measurement of Sample 1 B was done in air.

	Measurement	Ingrowth [mBq]	Counts/Time [mBq]
Sample 1 A	1	11.7 ± 0.3	12.1 ± 0.4
(3 rods)	2	9.8 ± 0.8	9.8 ± 2.0
Sample 1 B (3 rods)	1	15.5 ± 1.2	15.5 ± 0.6

Table 3.4: Copper coating measurement results. Sample 1 A is half of Sample 1 coated with copper using the plasma coating technique. Sample 1 B is the other half of Sample 1, only partially coated with copper using the same technique.

Now we want to compare the ^{220}Rn activity of the sample before and after coating. In table 3.5 we calculated the average activity before and after coating and multiplied the coated result by a factor of 2 to compare the estimated result for six electrodes. The achieved reduction factor is $(54 \pm 3)\%$. The reduction factor achieved for Sample 1 B is about 34%. This is in agreement with the 54%, if we take into account, that they are only partly coated.

	Not Coated [mBq]	Coated [mBq]	Reduction Factor
Sample 1/1 A	47.1 ± 0.4	21.7 ± 1.1	$(54 \pm 3)\%$

Table 3.5: Emanation reduction factor achieved by copper coating. The values are averaged from table 3.3 and 3.4.

Titanium Coated Sample

Sample 2 A, that was already measured as shown in Table 3.3, was coated with titanium using the PVD coating technique explained in Section 3.2. The titanium coated tungsten electrodes were only examined using the optical microscope. The observed structure of the coated and uncoated electrodes can be seen in Figure 3.11. The titanium seems so have formed a much smother layer compared to copper. There are no visible spots or cracks and the surface structure of the uncoated tungsten electrode is still visible.

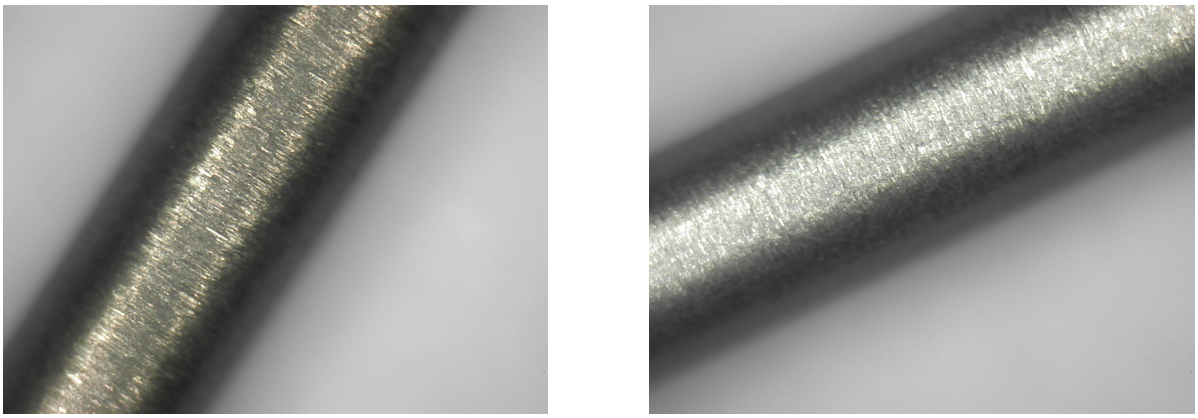

(a) Before Coating. **(b)** After Coating.

Figure 3.11: Microscope images of WTh(4%) welding electrodes before and after coating with titanium.

Again the measurements were repeated. The results are shown in Table 3.6. Measurement 3 was done in nitrogen, but we observed a leak. Measurement 4 was done in air with a small bowl of water inside the radon monitor to test the effect of humidity.

	Measurement	Ingrowth [mBq]	Counts/Time [mBq]
Sample 2 A	3	13.8 ± 1.2	13.8 ± 0.4
(3 rods)	4	15.2 ± 0.8	15.2 ± 0.3

Table 3.6: Titanium coating measurement results.

In Table 3.7 the activity of the sample before and after being coated with titanium are compared. The average value of the measurements from Table 3.3 and Table 3.6 are used to calculate the achieved reduction factor. The reduction factor is estimated to be $(32 \pm 1)\%$.

	Not Coated [mBq]	Coated [mBq]	Reduction Factor
Sample 2 A Average	21.4 ± 0.2	14.5 ± 0.4	$(32 \pm 1)\%$

Table 3.7: Emanation reduction factor achieved by titanium coating. The values are averaged from table 3.3 and 3.6.

3.4.5 Summary and Discussion of Results

In Table 3.8 the reduction factors are summarised. The reduction caused by coating the samples with copper is higher than the one obtained by coating the samples with titanium. In the course of these measurements, a complete reduction of the radon emanation was not achieved.

	Not Coated [mBq]	Coated [mBq]	Reduction Factor
Copper Coating (Average, 6 rods)	47.1 ± 0.4	21.7 ± 1.1	$(54 \pm 3)\%$
Titanium Coating (Average, 3 rods)	21.4 ± 0.2	14.5 ± 0.4	$(32 \pm 1)\%$

Table 3.8: Emanation reduction factor achieved by different coating techniques. The values are averaged from table 3.3, 3.4 and Table 3.6.

We discuss possible explanations, why radon still emanates from the samples. As was explained before, there are two processes causing radon emanation: Nuclear recoil and diffusion. The recoiled radon atoms have a kinetic energy in the order of 100 keV [20]. Therefore, they can penetrate materials up to a certain depth. In [21] this depth was found to be around 15 nm for stainless steel. We therefore assume that it is in the same order of magnitude for copper and titanium. As stated in Section 3.2, the achieved thickness for copper was estimated to be $\sim$1 μm and for titanium $\sim$(400-800) nm. Comparing the penetration depth with the coating thicknesses we presume that the effect of nuclear recoil should be completely prevented. Accordingly, the radon emanation that is still observed should be due to diffusion. It could be the case that in the process of coating, using the PVD coating technique, some kind of channels form along the surface of the samples. The titanium forms the coated layer by condensation. Therefore the vaporised titanium could favour to condensate on spaces, where titanium is already present, forming some kind o columns. Since we have no precise microscope images to observe effects on this small scale, we cannot conclude anything yet. There is also no conclusive result why the coated copper layer did not entirely block the radon emanation. Further studies have to be done, in order to fully understand this effect.

Summary and Conclusions

In the course of this bachelor thesis, the effect of surface coating on the radon emanation was investigated. It was carried out for a possible application in the XENON1T or XENONNT *dark matter* experiment, aiming for the direct detection of Weakly Interacting Massive Particles (WIMPs), using liquid xenon as a target material. The radioactive isotope ^{222}Rn is one of the most serious, intrinsic background sources, since it permanently emanates from all the detector materials applied in the XENON detectors.

In the first chapter, the nature of *dark matter* was introduced, starting off with cosmological evidences indicating its existence. Furthermore, the requirements that a *dark matter* particle would have to fulfil were stated and WIMPs, as a very promising model, was explained. After the detection principle of the dual-phase TPC was briefly depicted, radon, as one of the most crucial background sources in the XENON1T *dark matter* experiment, was introduced.

A set of ^{222}Rn measurements, performed using a miniaturized proportional counter, were discussed in the second chapter. The miniaturized proportional counters are important tools that are used to measure the radon emanation rates of different materials and detector parts in order to choose those with the lowest radon emanation. The final results of these measurements was an estimation of the detection efficiency of the proportional counters for the α-decays of the isotopes ^{222}Rn, ^{218}Po and ^{214}Po. It was found to be $(70 \pm 7)\%$ for ^{222}Rn, $(38 \pm 6)\%$ for ^{218}Po and $(38 \pm 5)\%$ for ^{214}Po.

In the third chapter we investigated if coating a material with a radio-pure layer could block radon from emanating. The aim was to find out if material coating could be a new approach to reduce background in XENON1T and the future upgrade XENONNT. First, the emanation process and the resulting specifications for the coating was illustrated. Second, the two coating materials copper and titanium were introduced in addition to the two different coating techniques that were utilised. A radon monitor was used for the emanation measurements done in this chapter. The setup including the working principle of the radon monitor was presented and the samples were shown. The samples are thoriated, tungsten welding electrodes, that emanate ^{220}Rn. In the second half of the chapter the results of the radon monitor measurements were presented. The energy calibration method was explained, followed by a detailed analysis of the observed energy spectrum. Two systematic effects of the radon monitor were investigated: The linearity of the

energy scale and the behaviour of the detection efficiency depending on humidity. Finally, the emanation rates measured for samples before and after coating were stated and the reduction factor achieved by coating was calculated. For the samples coated with titanium a reduction factor of $(32 \pm 1)\%$ was reached. Coating a sample with copper, on the other hand, accomplished a reduction factor of $(53 \pm 3)\%$.

Finally, we discuss the applicability of the results found in the course of this thesis. It is not clear, that the achieved reduction for the ^{220}Rn emanation rate implies, that it would also work for ^{222}Rn. The effect of nuclear recoil should be similar for both atoms, since their chemical properties are similar. They are also both gaseous at standard conditions, but the main difference is that the half-life of ^{220}Rn, with $T_{1/2}^{220Rn} = 55\,\mathrm{s}$ [8], is much shorter than the half-life of ^{222}Rn ($T_{1/2}^{222Rn} = 3.82\,\mathrm{d}$). Since a longer half-life leaves more time for diffusion, ^{222}Rn should therefore have different diffusive properties. The second difference between the measurements and the application in XENON1T or XENONNT is that we used tungsten samples to test the effect of coating, even though the majority of the detector parts are made of stainless steel. Stainless steel might behave differently during the coating process, since its material properties differ from tungsten. On top of that it has not been tested how copper or titanium stick to a stainless steel surface.

Concluding from these two arguments, we can say, that in order to find out if the ^{222}Rn emanation rate can be reduced by applying a surface coating to the contaminated detector materials in XENON1T, further studies have to be done. A ^{222}Rn sample on a stainless steel surface would provide the best sample for this purpose. Maybe additional coating materials should be considered. Additionally, the emanation measurements could be performed using the proportional counters, to receive very precise emanation rates.

Lastly, we use the results of this thesis, to estimate how the background of the XENON1T detector could be improved. The total ER background was estimated to be $(1.80 \pm 0.15) \cdot 10^{-4}$ (kg·day·keV)$^{-1}$ in a 1 t fiducial volume [7]. About 85% ($1.54 \cdot 10^{-4}$ (kg·day·keV)$^{-1}$[10]) of this originate from ^{222}Rn. Using the individual emanation rates of the XENON1T components, that were determined in [13], we can say that, about 46% of the radon contamination emanates from detector components that could be coated to prevent emanation. These consist mainly of stainless steel pipes and the cryostat itself. If we now assume a radon emanation reduction of 54%, and take into account that the ER background scales linear with the total ^{222}Rn concentration as shown in [22], we can estimate the reduced ER background contribution from ^{222}Rn to be $1.16 \cdot 10^{-4}$ (kg·day·keV)$^{-1}$. It was therefore reduced by ∼25%. This would lead to a reduced total ER background of $1.42 \cdot 10^{-4}$ (kg·day·keV)$^{-1}$. The total reduction would therefore be about 22%.

If we assume a radon emanation reduction of 100% we would be able to reduce the ER background contribution from ^{222}Rn by around 46% (to $0.84 \cdot 10^{-4}$ (kg·day·keV)$^{-1}$) and the total ER background by ∼39% (to $1.1 \cdot 10^{-4}$ (kg·day·keV)$^{-1}$).

Appendix A

Derived Decay Functions of Subsequent Decays (^{222}Rn)

A.1 Functions describing the Ingrowth

$$N_A(t) = N_A^0 e^{-\lambda_a t} \tag{A.1}$$

$$N_B(t) = N_A^0 \lambda_a \left(\left(\frac{e^{-\lambda_a t}}{\lambda_b - \lambda_a} \right) + \left(\frac{e^{-\lambda_b t}}{\lambda_a - \lambda_b} \right) \right) \tag{A.2}$$

$$N_C(t) = N_A^0 \lambda_a \lambda_b \left(\frac{e^{-\lambda_a t}}{(\lambda_b - \lambda_a)(\lambda_c - \lambda_a)} + \frac{e^{-\lambda_b t}}{(\lambda_a - \lambda_b)(\lambda_c - \lambda_b)} + \frac{e^{-\lambda_c t}}{(\lambda_a - \lambda_c)(\lambda_b - \lambda_c)} \right) \tag{A.3}$$

$$N_D(t) = N_A^0 \lambda_a \lambda_b \lambda_c C_1(t) \tag{A.4}$$

$$\begin{aligned} C_1(t) = & \frac{e^{-\lambda_a t}}{(\lambda_b - \lambda_a)(\lambda_c - \lambda_a)(\lambda_d - \lambda_a)} + \frac{e^{-\lambda_b t}}{(\lambda_a - \lambda_b)(\lambda_c - \lambda_b)(\lambda_d - \lambda_b)} \\ & + \frac{e^{-\lambda_c t}}{(\lambda_a - \lambda_c)(\lambda_b - \lambda_c)(\lambda_d - \lambda_c)} + \frac{e^{-\lambda_c t}}{(\lambda_a - \lambda_d)(\lambda_b - \lambda_d)(\lambda_c - \lambda_d)} \end{aligned} \tag{A.5}$$

$$N_E(t) = N_A^0 \lambda_a \lambda_b \lambda_c \lambda_d C(t) \tag{A.6}$$

$$\begin{aligned} C(t) = & \frac{e^{-\lambda_a t}}{(\lambda_b - \lambda_a)(\lambda_c - \lambda_a)(\lambda_d - \lambda_a)(\lambda_e - \lambda_a)} \\ & + \frac{e^{-\lambda_b t}}{(\lambda_a - \lambda_b)(\lambda_c - \lambda_b)(\lambda_d - \lambda_b)(\lambda_e - \lambda_b)} + \frac{e^{-\lambda_c t}}{(\lambda_a - \lambda_c)(\lambda_b - \lambda_c)(\lambda_d - \lambda_c)(\lambda_e - \lambda_c)} \\ & + \frac{e^{-\lambda_d t}}{(\lambda_a - \lambda_d)(\lambda_b - \lambda_d)(\lambda_c - \lambda_d)(\lambda_e - \lambda_d)} + \frac{e^{-\lambda_e t}}{(\lambda_a - \lambda_e)(\lambda_b - \lambda_e)(\lambda_c - \lambda_e)(\lambda_d - \lambda_e)} \end{aligned} \tag{A.7}$$

Appendix B

Derived Decay Functions of Subsequent Decays (^{220}Rn)

B.1 Functions describing the Ingrowth

$$N_A(t) = N_A^0 = const \tag{B.1}$$

$$N_B(t) = \frac{N_A^0 \lambda_a}{\lambda_b} \left(1 - e^{-\lambda_b t}\right) \tag{B.2}$$

$$N_C(t) = \frac{N_A^0 \lambda_a}{\lambda_b - \lambda_c} \left(e^{-\lambda_b t} - e^{-\lambda_c t}\right) + \frac{N_A^0 \lambda_a}{\lambda_c} \left(1 - e^{-\lambda_c t}\right) \tag{B.3}$$

$$\begin{aligned} N_D(t) = &\frac{N_A^0 \lambda_a \lambda_c}{(\lambda_b - \lambda_c)(\lambda_d - \lambda_b)} \left(e^{-\lambda_b t} - e^{-\lambda_d t}\right) \\ &+ \frac{N_A^0 \lambda_a \lambda_b}{(\lambda_b - \lambda_c)(\lambda_c - \lambda_d)} \left(e^{-\lambda_c t} - e^{-\lambda_d t}\right) + \frac{N_A^0 \lambda_a}{\lambda_d} \left(1 - e^{-\lambda_d t}\right) \end{aligned} \tag{B.4}$$

B.2 Functions describing the Decay

$$N_A(t) = N_A^0 e^{-\lambda_a t} \tag{B.5}$$

$$N_B(t) = \frac{N_A^0 \lambda_a}{\lambda_b - \lambda_a} \left(e^{-\lambda_a t} - e^{-\lambda_b t}\right) + N_B^0 \left(e^{-\lambda_b t}\right) \tag{B.6}$$

$$\begin{aligned} N_C(t) = &\frac{N_A^0 \lambda_a \lambda_b}{(\lambda_b - \lambda_a)(\lambda_c - \lambda_a)} \left(e^{-\lambda_a t} - e^{-\lambda_c t}\right) \\ &+ \frac{(N_A^0 \lambda_a \lambda_b) + (N_B^0 \lambda_a \lambda_b) - (N_B^0 \lambda_b^2)}{(\lambda_a - \lambda_b)(\lambda_c - \lambda_b)} \left(e^{-\lambda_b t} - e^{-\lambda_c t}\right) + N_C^0 e^{-\lambda_c t} \end{aligned} \tag{B.7}$$

Appendix C

Scanning Electron Microscope Images of Coated WTh(4%) Electrodes

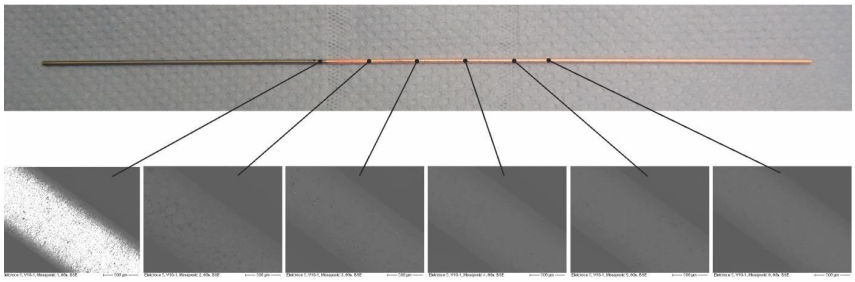

Figure C.1: Half coated welding electrode.

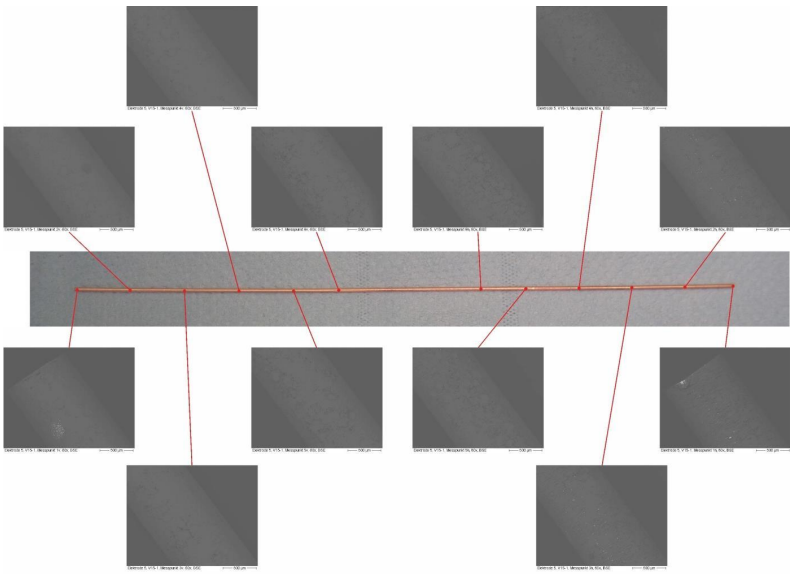

Figure C.2: Fully coated welding electrode.

Bibliography

[1] F. Zwicky, "Die Rotverschiebung von extragalaktischen Nebeln," *Helvetica Physica Acta*, vol. 6, pp. 110–127, 1933.

[2] V. C. Rubin, N. Thonnard, and W. K. Ford, Jr., "Extended rotation curves of high-luminosity spiral galaxies. IV - Systematic dynamical properties, SA through SC," vol. 225, pp. L107–L111, Nov. 1978.

[3] P. A. R. Ade *et al.*, "Planck 2013 results. I. Overview of products and scientific results," *Astron. Astrophys.*, vol. 571, p. A1, 2014.

[4] H. Baer and X. Tata, "Dark matter and the LHC," in *Physics at the Large Hadron Collider* (A. Datta, B. Mukhopadhyaya, A. Raychaudhuri, A. K. Gupta, C. L. Khetrapal, T. Padmanabhan, and M. Vijayan, eds.), pp. 179–203, 2009.

[5] D. Clowe, M. Bradac, A. H. Gonzalez, M. Markevitch, S. W. Randall, C. Jones, and D. Zaritsky, "A direct empirical proof of the existence of dark matter," *Astrophys. J.*, vol. 648, pp. L109–L113, 2006.

[6] E. Aprile and XENON1T collaboration, "The XENON1T Dark Matter Search Experiment," *ArXiv e-prints*, June 2012.

[7] E. Aprile *et al.*, "Physics reach of the XENON1T dark matter experiment," *JCAP*, vol. 1604, no. 04, p. 027, 2016.

[8] M.-M. Bé, V. Chisté, C. Dulieu, E. Browne, V. Chechev, N. Kuzmenko, R. Helmer, A. Nichols, E. Schönfeld, and R. Dersch, *Table of Radionuclides*, vol. 2 of *Monographie BIPM-5*. Pavillon de Breteuil, F-92310 Sèvres, France: Bureau International des Poids et Mesures, 2004.

[9] M.-M. Bé, V. Chisté, C. Dulieu, E. Browne, V. Chechev, N. Kuzmenko, F. Kondev, A. Luca, M. Galán, A. Pearce, and X. Huang, *Table of Radionuclides*, vol. 4 of *Monographie BIPM-5*. Pavillon de Breteuil, F-92310 Sèvres, France: Bureau International des Poids et Mesures, 2008.

[10] E. Aprile *et al.*, "Physics reach of the XENON1T dark matter experiment," *JCAP*, vol. 1604, no. 04, p. 027, 2016.

[11] S. Brünner, "Study of radon adsorption on activated carbon for a purification system in XENON1T," diploma, Karl-Franzens-Universität, Graz, 2013.

[12] G. Zuzel and H. Simgen, "High sensitivity radon emanation measurements," *Applied Radiation and Isotopes*, vol. 67, no. 5, pp. 889 – 893, 2009. 5th International Conference on Radionuclide Metrology - Low-Level Radioactivity Measurement Techniques ICRM-LLRMT'08.

[13] N. Rupp, "On the detection of ^{222}Rn with miniaturized proportional counters: background, sensitivity studies and results for XENON1T," master, Ruprecht-Karls-Universität, Heidelberg, 2015.

[14] P. Pagelkopf and J. Porstendörfer, "Neutralisation rate and the fraction of the positive 218po-clusters in air," *Atmospheric Environment*, vol. 37, no. 8, pp. 1057 – 1064, 2003.

[15] H. Simgen, F. Arnold, H. Aufmhoff, R. Baumann, F. Kaether, S. Lindemann, L. Rauch, H. Schlager, C. Schlosser, and U. Schumann, "Detection of 133xe from the fukushima nuclear power plant in the upper troposphere above germany," *Journal of Environmental Radioactivity*, vol. 132, pp. 94 – 99, 2014.

[16] M. Friedel. internal report.

[17] S. Lindemann, *Reinigung und Nachweis von Edelgasen mit miniaturisierten Proportionalzählrohren*. PhD thesis, Ruprecht-Karls Universität Heidelberg Heidelberg, 2009.

[18] D. L. P. GmbH, "High-energy arc plasma." [Online; accessed 29-July-2016].

[19] EC Europ Coating GmbH, "Pvd coating." [Online; accessed 25-August-2016].

[20] H. Simgen. personal communication.

[21] I. F. M.-Q.Liu, H. Lee and A. McDonald, "Radon Emanation from Stainless Steel," *SNO Technical Reports*, no. 075, 1990.

[22] E. Aprile *et al.*, "Study of the electromagnetic background in the XENON100 experiment," vol. 83, p. 082001, Apr. 2011.

List of Figures

List of Tables

Erklärung

Ich versichere, dass ich diese Arbeit selbstständig verfasst und keine anderen als die angegebenen Quellen und Hilfsmittel benutzt habe.

Heidelberg, den 30.08.2016

Leander Fischer